Manipulating pseudospin-polarized state of light in dispersion-immune photonic topological metacrystals

Xiao-Dong Chen, Zi-Lan Deng, Wen-Jie Chen, Jia-Rong Wang, and Jian-Wen Dong*
State Key Laboratory of Optoelectronic Materials and Technologies and School of Physics and Engineering, Sun Yat-Sen University, Guangzhou 510275, China
(Received 18 March 2015; revised manuscript received 5 July 2015; published 30 July 2015)

We propose a scheme that the material dispersion can be immune in a kind of photonic topological metacrystal with uniform permittivity and permeability but staggered bianisotropy. The topological behaviors can be maintained even though the metamaterials are intrinsically dispersive. A nontrivial topological band gap with a large gap spin Chern number is confirmed in such dispersion-immune photonic topological metacrystals. Two proposals of a robust pseudospin-polarized power splitter and a slow-light waveguide show evidence on the manipulation of the pseudospin-momentum locked states in a backscattering-free manner. In addition, a realistic design of a nontrivial dispersion-immune photonic metacrystal is also issued and discussed.

DOI: 10.1103/PhysRevB.92.014210 PACS number(s): 42.70.Qs, 03.65.Vf, 81.05.Xj, 42.25.Bs

I. INTRODUCTION

Manipulating frequency, polarization, and phase is a feasible and efficient way to control flow of electromagnetic waves in light science and application [1–6]. For example, negative refracted light-beam steering was realized in optical metamaterials by tuning the frequency of incident light [2]. Unidirectional coupling was achieved in a metasurface by controlling the polarization of incident light [6]. In those cases, the polarization of the output light is independent of the momentum of photon and thus it cannot be distinguished by different flow direction of light. Topological photonics [7–27], which originated from the concept of topological protection in condense matter, brings a breakthrough on such topic. Nontrivial topological protected edge states have been found in many photonic topological band gap systems, for example, magnetic photonic crystals [9–13], bianisotropic-based photonic topological insulators [14–16], resonating lattices [17–20], evanescently coupled helical waveguides [21,22], and gyroid photonic crystals [23]. In certain systems, the exotic edge states will become pseudospin-momentum entangled, meaning that the direction of light is locked to the pseudospin polarization. The pseudospin-momentum locked state provides a new degree of freedom to manipulate electromagnetic waves in photonic devices. Further, photonic topological behavior benefits on overcoming propagation loss in disorder senstitive structures, such as slow-light and Anderson localization in photonic crystal waveguides. However, the photonic topological properties can be weakened and sometimes may be eliminated by the material dispersion, which is inevitable due to the law of causality. It is of great importance to cope with such an intrinsic material dispersion in photonic topological systems.

In this paper, we propose a kind of photonic topological metacrystals in which the material dispersions can be immune. We have constructed a triangular photonic metacrystal with uniform permittivity and permeability but staggered bianisotropy, in which the ε/μ-matching condition is naturally fulfilled as only one bianisotropic material is used. Originated from modes exchange at high-symmetry k points, a topological phase transition and a nontrivial band gap with a large gap spin Chern number have been realized in the dispersion-immune photonic topological metacrystals. Robust pseudospin-polarized power splitter and slow-light waveguide are discussed to show the ability of manipulating the pseudospin-momentum locked states of light. Lastly, a realistic experimental proposal of nontrivial staggered photonic metacrystal is designed.

II. DISPERSION-IMMUNE PHOTONIC TOPOLOGICAL METACRYSTAL

Photonic topological metacrystals can be realized in bianisotropic photonic metacrystals in which nontrivial photonic gaps are derived from the cross coupling of transverse electric (TE) and transverse magnetic (TM) polarized modes. The cross couplings can be achieved by introducing either realistic or effective bianisotropy. Pure pseudospin-up/pseudospin-down states can be formed by the in-phase/out-of-phase TE-TM coupled modes in a metacrystal when the ε/μ-matching condition is satisfied. But such condition is mostly too harsh to be fulfilled due to the intrinsic material dispersion. A representative configuration [left in Fig. 1(a)] is constructed by bianisotropic rods (green with down arrows) sitting in a nonbianisotropic background material (purple). Each material has its own set of dispersive constitutive parameters, and thus the ε/μ-matching condition will be fulfilled just at the frequency of ω_0, while broken down away from ω_0 [middle in Fig. 1(a)]. It will result in the nondegeneration of TE and TM polarized modes and the mixture between pseudospin-up and pseudospin-down states [right in Fig. 1(a)]. If the ε/μ mismatch becomes much more serious, the topological band gap will even close. But such dilemma can be removed by using the idea of staggered arrangement. As illustrated in the left panel of Fig. 1(b), the staggered photonic topological metacrystal is constructed by only one kind of metamaterial with uniform permittivity and permeability but opposite bianisotropic coefficient in the "rod" and "background" regions, corresponding to the up and down arrows in Fig. 1(b). It is obvious that the

*Now visiting University of California, Berkeley, California; dongjwen@mail.sysu.edu.cn

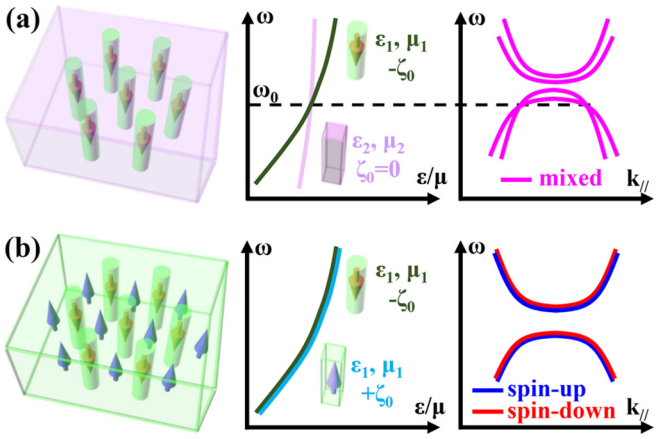

FIG. 1. (Color online) Schematic of two different structures to achieve photonic topological insulators. (a) Bianisotropic photonic metacrystals consisting of highly dispersive bianisotropic rods (green with down arrows) and nonbianisotropic background (purple). The ε/μ-matching condition can just be satisfied at the cross point of ω_0, resulting in the mixture of pseudospin-up and pseudospin-down modes. (b) Dispersion-immune photonic topological insulators: staggered photonic metacrystals consisting of uniform permittivity and permeability (green) but opposite bianisotropy (different arrow direction) in the "rod" and "background" regions. Although it is highly dispersive, the ε/μ-matching condition is naturally fulfilled, and thus the photonic topological band gap does not have an effect. Note that the small shift in the middle and right panels of (b) is for better visualization only.

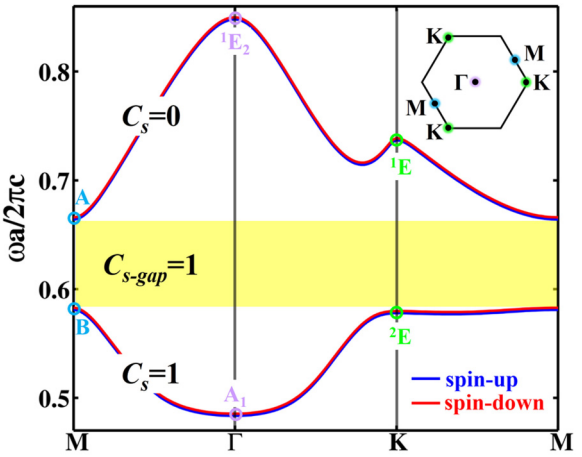

FIG. 2. (Color online) Photonic band structure of triangular staggered photonic metacrystals constructed by dispersive metamaterials. A Drude model is applied to the metamaterial as a typical frequency-dependent relation. The losses of metamaterials are ignored to simplify the numerical simulation. The metamaterials have opposite bianisotropic response between the rod and the background. Both doubly degenerate bulk bands and topologically nontrivial band gaps are found in this dispersion-immune photonic topological insulator. The spin Chern number of each band is determined by analyzing the irreducible representations of eigenmodes at high-symmetry k points and obtaining the corresponding C_n-rotation eigenvalues.

ε/μ-matching condition can be automatically fulfilled at each frequency even if the metamaterial is highly dispersive [middle in Fig. 1(b)]. The resultant band gap is derived by Bragg scattering of periodic bianisotropy. It does not suffer from the frequency dispersion, which distinguishes from the band gaps born of periodic permittivity and permeability potentials. Consequently, the photonic topological band gap is immune to the material dispersion of the bianisotropic metamaterial. Note that the opposite bianisotropy can be realized by flipping the orientation of the split-ring resonators which will be shown in Sec. III E and Fig. 8.

Next we consider a concrete numerical example of triangular staggered photonic metacrystal in order to confirm the dispersion-immune concept. The unit cell of the metacrystal consists of a rod with a radius of $0.3a$ embedded in the background material, where a is the lattice constant. All materials are bianisotropy with the reciprocal constitutive relations of $\vec{\mathbf{D}} = \varepsilon_0 \overleftrightarrow{\boldsymbol{\varepsilon}}_{\mathbf{r}} \vec{\mathbf{E}} + \overleftrightarrow{\zeta} \vec{\mathbf{H}}$ and $\vec{\mathbf{B}} = \mu_0 \overleftrightarrow{\boldsymbol{\mu}}_{\mathbf{r}} \vec{\mathbf{H}} + \overleftrightarrow{\zeta} \vec{\mathbf{E}}$. Here, $\overleftrightarrow{\zeta}$ is the magnetoelectric coefficient tensor with nonzero elements of $\zeta_{12} = \zeta_{21}^* = i\zeta_0/c$. $\overleftrightarrow{\boldsymbol{\varepsilon}}_{\mathbf{r}}$ and $\overleftrightarrow{\boldsymbol{\mu}}_{\mathbf{r}} = \overleftrightarrow{\boldsymbol{\varepsilon}}_{\mathbf{r}}/\alpha = \mathrm{diag}(\mu_{r\parallel}, \mu_{r\parallel}, \mu_{rz})$ are the relative permittivity and permeability, where α is a constant. In order to demonstrate the dispersion-immune concept, we assume the numerically artificial frequency-dependent formula: $\overleftrightarrow{\boldsymbol{\varepsilon}}_{\mathbf{r}}(\omega) = 2 - (1.1\pi c/\omega a)^2$ and $\overleftrightarrow{\boldsymbol{\mu}}_{\mathbf{r}} = 1$ for all metamaterials. The losses of metamaterials are ignored to simplify the numerical simulation. It is noted that the dispersion-immune concept in the staggered photonic metacrystals would work no matter what frequency-dependent model is applied to the constituent materials. The staggered binisotropy is set as $\zeta_0 = -0.84$ in the "rod" and $\zeta_0 = 0.84$ in the background. Figure 2 shows two lowest bulk bands calculated by adding bianisotropic constitutive equations into COMSOL Multiphysics. The time-reversal pair of pseudospin-polarized states can be retrieved by introducing the pseudofields $(\vec{\mathbf{P}}^+, \vec{\mathbf{P}}^-) \equiv (\sqrt{\alpha\varepsilon_0}\,\vec{\mathbf{E}} + \sqrt{\mu_0}\,\vec{\mathbf{H}}, \sqrt{\alpha\varepsilon_0}\,\vec{\mathbf{E}} - \sqrt{\mu_0}\,\vec{\mathbf{H}})$. The pseudospin-up/pseudospin-down state has the form of $(P_x^{\mp}, P_y^{\mp}, P_z^{\pm})^T$ because the full-vector Maxwell equations can be decomposed into two decoupled subspaces, i.e.,

$$\nabla \times \begin{pmatrix} P_x^- \\ P_y^- \\ P_z^+ \end{pmatrix} = -i\frac{\omega}{c} \begin{pmatrix} \mu_{r\parallel}\sqrt{\alpha} & i\zeta_0 & \\ -i\zeta_0 & \mu_{r\parallel}\sqrt{\alpha} & \\ & & -\mu_{rz}\sqrt{\alpha} \end{pmatrix} \begin{pmatrix} P_x^- \\ P_y^- \\ P_z^+ \end{pmatrix}, \tag{1}$$

$$\nabla \times \begin{pmatrix} P_x^+ \\ P_y^+ \\ P_z^- \end{pmatrix} = i\frac{\omega}{c} \begin{pmatrix} \mu_{r\parallel}\sqrt{\alpha} & -i\zeta_0 & \\ i\zeta_0 & \mu_{r\parallel}\sqrt{\alpha} & \\ & & -\mu_{rz}\sqrt{\alpha} \end{pmatrix} \begin{pmatrix} P_x^+ \\ P_y^+ \\ P_z^- \end{pmatrix}. \tag{2}$$

Figure 2 illustrates that each band is doubly degenerate, even when the bianisotropic material is dispersive. A photonic band gap is found within the normalized frequency ranges of 0.58–0.66 (yellow). To characterize the topological feature, we calculate the spin Chern number of each band. In principle, the spin Chern number of the mth bulk band (C_s^m) can be calculated with the determinant of the closed loop integral of

the Berry connection along the boundary of the Brillouin zone. When photonic crystals are C_n invariant, Berry connections at the C_n-rotation connected k points are equal. So one just needs to integrate the Berry connection along the boundary of the irreducible Brillouin zone and get one-nth of the Berry phase (i.e., $2\pi C_s^m/n$). Due to the periodicity of the irreducible Brillouin zone and the C_n invariance, the determinant of the closed loop integral can be evaluated with the determinant of the sewing matrix at high-symmetry reciprocal k points [28]. For the triangular lattice, one can determine the spin Chern number as follows:

$$e^{i[(2\pi/6)C_s^m]} = e^{i[(2\pi/6)C_m^+]} = \eta_m^+(\Gamma)\theta_m^+(K)\gamma_m^+(M), \qquad (3)$$

where $\eta^+(\Gamma)$, $\theta^+(K)$, and $\gamma^+(M)$ represent the eigenvalues of C_6, C_3, and C_2 rotation operators on the pseudospin-up modes at Γ, K, and M points, respectively. Analyzing the irreducible representations of eigenmodes at high-symmetry k points helps to obtain the corresponding C_n-rotation eigenvalues illustrated in Fig. 2. Note that one should change the field patterns in COMSOL results to their conjugated parts because we assume the harmonic time dependence to be $e^{-i\omega t}$. Note also that one should do the rotation operator on the pseudospin-up polarized mode which refers to the pseudofields $(P_x^{\mp}, P_y^{\mp}, P_z^{\pm})^T$. Results show that the spin Chern number of the two lowest bands is 1 and 0, respectively. Therefore, the gap spin Chern number ($C_{s\text{-gap}} = \sum_m C_s^m$) is 1 for the lowest band gap, indicating that the band gap is topologically nontrivial. In short, the staggered photonic metacrystal can serve as a dispersion-immune photonic topological insulator, even if the constitutive materials are dispersive.

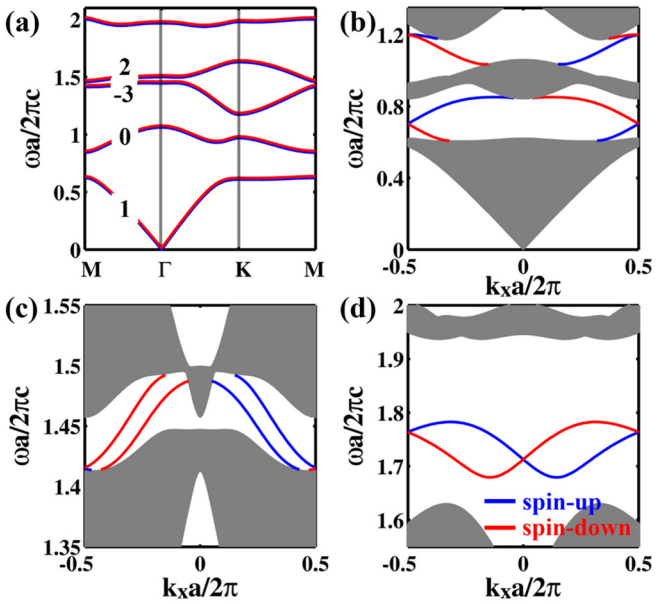

FIG. 3. (Color online) Bulk bands and pseudospin-momentum locked edge state in triangular staggered photonic metacrystals. (a) Bulk bands with spin Chern number for $\zeta_0 = 0.84$. The nondispersive "air" configuration is assumed. A nontrivial topological band gap with a large gap spin Chern number is found in the third band gap. (b)–(d) Pseudospin-momentum locked edge states along the ΓK direction in the four lowest band gaps, of which the topological characters are accurately predicted from the gap spin Chern number calculated by group theory.

III. RESULTS AND DISCUSSIONS

A. Pseudospin-momentum locked edge states

To generalize the dispersion-immune concept in staggered photonic metacrystals, we consider another bianisotropic medium with a relative permittivity of $\overleftrightarrow{\boldsymbol{\varepsilon}}_{\mathbf{r}}$ and a relative permeability of $\overleftrightarrow{\boldsymbol{\mu}}_{\mathbf{r}} = \overleftrightarrow{\boldsymbol{\varepsilon}}_{\mathbf{r}}/\alpha = \mathrm{diag}(\mu_{r\parallel}, \mu_{r\parallel}, \mu_{rz}) = \mathrm{diag}(\mu_{r\parallel}, \mu_{r\parallel}, \mu_{r\parallel}\beta)$, where α and β are constants. Due to the scaling law of Maxwell equations, eigenmodes of the material configuration $(\overleftrightarrow{\boldsymbol{\varepsilon}}_{\mathbf{r}}, \overleftrightarrow{\boldsymbol{\mu}}_{\mathbf{r}}, \overleftrightarrow{\boldsymbol{\zeta}})$ can be obtained by scaling down (or scaling up) those of the "air" configuration $(1, 1, \overleftrightarrow{\boldsymbol{\zeta}}/\mu_{r\parallel}\sqrt{\alpha})$, regardless of material dispersion. Therefore, without loss of generality, we apply the nondispersive "air" configuration for triangular staggered photonic metacrystals for simplification. Note that material dispersion does not change the topological feature [9,14,15] and the results in this paper are general for staggered photonic metacrystals with square or honeycomb lattices.

Figure 3(a) shows the bulk band structure of the dispersion-immune photonic topological metacrystal for $\zeta_0 = 0.84$. There are four photonic band gaps below the frequency of $2(c/a)$, which are characterized by the gap spin Chern numbers of 1, 1, -2, and 0, respectively. It indicates that the three lowest band gaps are topologically nontrivial as $C_{s\text{-gap}}$ is nonzero, while the fourth band gap is trivial. Meanwhile, the first two band gaps are topologically distinct from the third band gap because they have different gap spin Chern numbers. The topological distinction of the band gaps can be witnessed from the pseudospin-momentum locked edge states. To this end, we constructed an edge along the ΓK direction between the staggered photonic metacrystal and the trivial gap material which does not allow any electromagnetic energy to enter. For a realistic material point of view, there are two ways to achieve the trivial gap material. One is to use another photonic metacrystal with trivial complete band gap. A representative design is using an array of perfect electric conductor meta-atoms with different shape [15]. The other way may be using a gap material, so-called perfect electromagnetic conductor [29–31], which is out of the scope of this paper. For simplicity, the gap material is numerically set with $\overleftrightarrow{\boldsymbol{\varepsilon}}_{\mathbf{r}} = \overleftrightarrow{\boldsymbol{\mu}}_{\mathbf{r}} = \mathrm{diag}(1, 1, -10\,000)$ in the simulation. Figure 3(b) shows that there is only one gapless pseudospin-polarized edge state spanning the whole gap for the first two band gaps. It is consistent with the fact of $C_{s\text{-gap}} = 1$. The group velocities of pseudospin-up edge states (blue) point to the $+x$ direction, while those of pseudospin-down edge states (red) point to the $-x$ direction. These pseudospin-momentum locked edge states are similar to chiral edge states in quantum Hall systems with opposite external fields. For the third band gap with large gap spin Chern number to be -2, there should be two gapless edge states pointing to the directions opposite to those in the first two lowest band gaps [32]. This is also verified in Fig. 3(c). The origin of such large gap spin Chern number will be discussed in the next section. For comparison, the fourth band gap has zero gap spin Chern number, and thus the pseudospin edge

states are gapped and form a closed loop instead of a gapless connection [Fig. 3(d)].

B. Origin of topological band gap with large gap spin Chern number

Topological band gaps with a large gap spin Chern number enable multimode waveguides with increased mode density and higher coupling efficiency [13]. To investigate the origin of the nontrivial topological band gap with a large gap spin Chern number, we focus on the third band gap and plot the gap map as a function of ζ_0 in Fig. 4(c). One can see that such a gap map has three topological isolated phases, each of which cannot be adiabatically connected to its neighboring phase without closing and reopening the band gap. In order to visualize the phase transition, we plot the three-dimensional band structure near the critical transition point, as shown in Fig. 4(a), giving an indication of the closing and reopening of the gap. We also plot the mode evolutions at the Γ point in Fig. 4(b). When ζ_0 reaches 0.816, two modes with different irreducible representations are accidentally degenerate [red solid circle in Fig. 4(b)]. After the phase transition, they will exchange the sequence, resulting in the change from trivial gap ($C_{s\text{-gap}} = 0$) to nontrivial gap ($C_{s\text{-gap}} = -2$). Another similar topological phase transition occurs at $\zeta_0 = 0.858$ related to two nontrivial topological phases. Near the latter critical transition point, two different eigenmodes at the M point approach closer and closer, then exchange and move apart [Fig. 4(d)]. The bulk frequency band gap will close and reopen along with the change of gap spin Chern number [Fig. 4(e)]. As a result, the band gap becomes another nontrivial band gap.

C. Robust pseudospin-polarized power splitter

Dispersion-immune photonic topological metacrystals do benefit the applications of a polarization-controllable and disorder-insensitive photonic circuit. Here we discuss a pseudospin-polarized power splitter, as illustrated in Fig. 5. The power splitter is constructed by capping the triangular staggered photonic metacrystal with the gap material. A harmonic line H_z source $\mathbf{H} = H_z e^{-i\omega t}\hat{\mathbf{z}}$ (green) and a harmonic line E_z source $\mathbf{E} = E_z e^{-i\omega t}\hat{\mathbf{z}}$ (purple) are excited at the same spot on the left corner of the splitter. The operating frequency is set to be $0.71(c/a)$ at which the staggered photonic metacrystal behaves as a photonic topological insulator. The amplitude of the line H_z source is kept as the constant of $\sqrt{\mu_0/\varepsilon_0}$, while the line E_z source is assumed to change and it is used to excite pseudospin-polarized modes with different ratios. As a result, the power flow can be automatically selective to propagate along either the upper or lower waveguide port. For example,

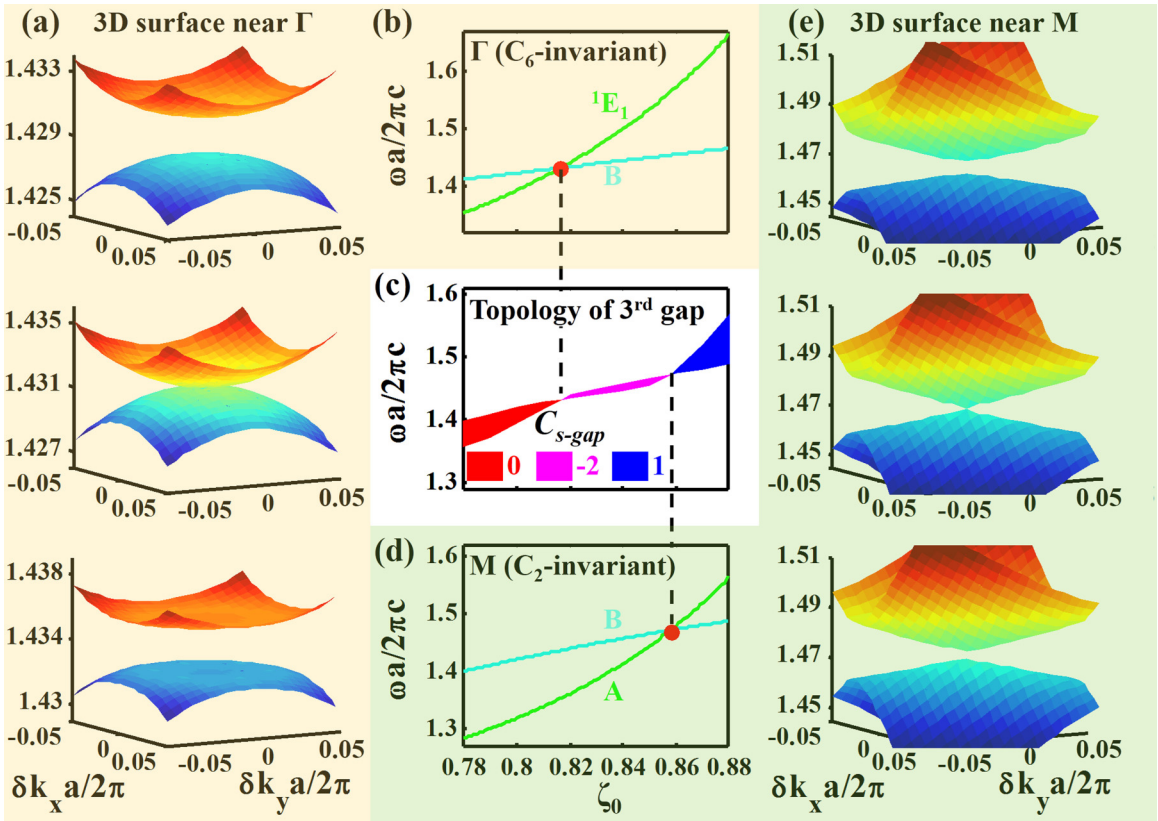

FIG. 4. (Color online) Origin of topological band gap with large gap spin Chern number. (a) Three dimensional eigenfrequency surfaces near the Γ point and (b) evolutions at the Γ point in the vicinity of $\zeta_0 = 0.816$ showing the closing and reopening of the third gap. Red circle in (b) marks the exchange point between two modes with different irreducible representations at the Γ point. (c) Gap map of the third band gap. Topological phase transition happens twice as the $C_{s\text{-gap}}$ takes two jumps of -2 and 3 due to mode exchange at the Γ and M points. Blue and pink represent nontrivial band gaps with $C_{s\text{-gap}} = 1$ and -2, while red represents trivial band gap with zero $C_{s\text{-gap}}$. (d) and (e) are similar to (b) and (a) but for another topological phase transition.

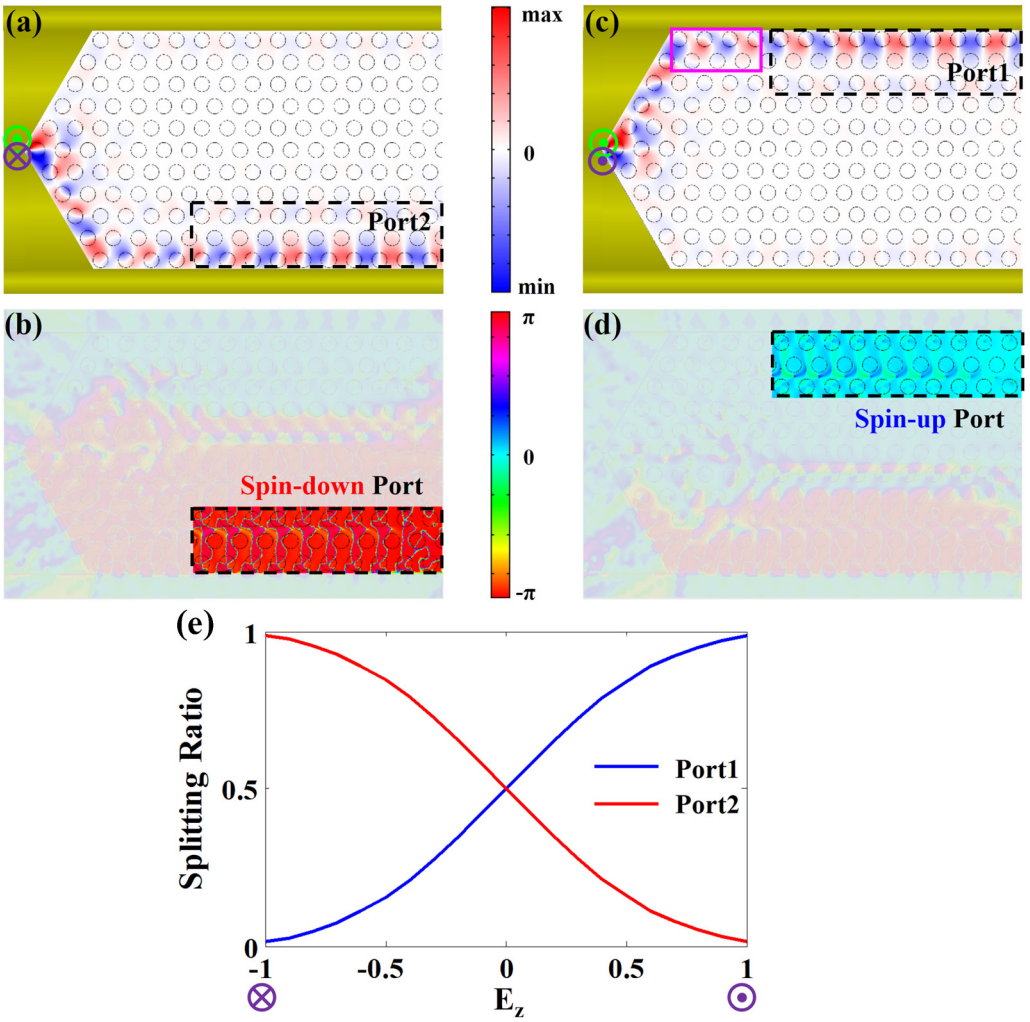

FIG. 5. (Color online) Pseudospin-polarized power splitter. An H_z point source (green) and an E_z point source (purple) with a frequency of $0.71(c/a)$ are excited at the same spot at the left-middle end of the splitter (source icons are shifted separately for clarity). The amplitude and direction of the H_z point source is kept as $\sqrt{\mu_0/\varepsilon_0}$, while those of the E_z point source is changed for selectively exciting pseudospin-polarized states with different ratios. The majority of excited electromagnetic waves proceeds to (a) port 2 when $E_z = -1$ and (c) port 1 when $E_z = 1$. (b) and (d) show the phase differences between the z components of electric and magnetic fields, indicating that port 2 and port 1 are pseudospin-down and pseudospin-up ports, respectively. The regions that do not carry useful information are shaded. (e) The splitting ratio as a function of the amplitude and direction of the E_z point source.

when $E_z = -1$, the majority of the power flow is modulated into the lower waveguide [port 2, Fig. 5(a)]. The phase difference between the z component of the electric field and the magnetic field along the lower waveguide is approximate to π (or equivalently $-\pi$) [highlighted part in Fig. 4(b)]. When E_z changes from -1 to 1, the source changes to be pseudospin-up, and consequently, the flow of light is manipulated from port 2 to port 1 [Fig. 5(c)]. The phase difference along the upper waveguide turns to be zero [Fig. 5(d)]. Figure 5(e) and the online video [33] show a much more complete picture on the pseudospin-polarized power splitter.

Next, we investigate the robust transport behavior in the pseudospin-polarized power splitter. Figure 6 shows the field patterns of the z component of the electric field with the excitation of pseudospin-up source in the presence of various kinds of defects. Here, we introduce a lightning-shaped opaque obstacle [Fig. 6(a)], missing rods [Fig. 6(b)], and shifting rods [Fig. 6(c)] into the upper waveguide. We see that the electromagnetic waves can go around the defects and keep moving rightward. Further, we also see that there is no Fabry-Pérot interference fringe on the left of the defects [see the zoom-in parts in Figs. 5(a)–5(c)], indicating that the pseudospin-polarized power splitter is backscattering-free and the waveguide channel is robust. A more complicated defect is presented with the combination of the above three defects. Again, we find the robust transport behavior in Fig. 6(d). The robustness of the spin-polarized power splitter is topologically protected by the photonic topological insulator.

D. Slow-light waveguide

In this section, we discuss the potential application of slow light in dispersion-immune photonic topological metacrystals. The slow-light waveguide is constructed by capping the

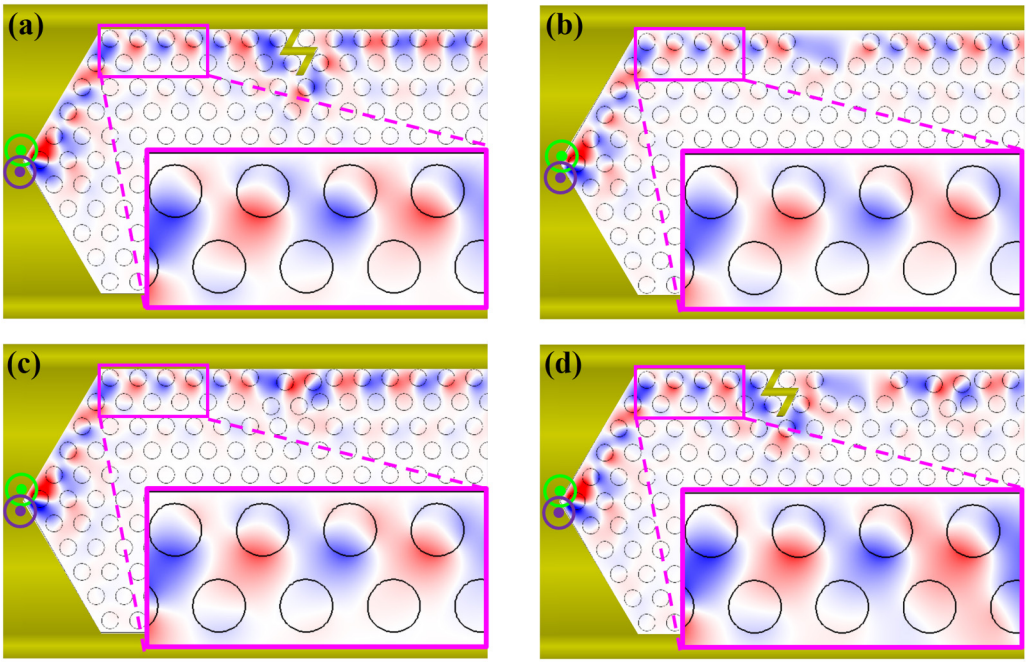

FIG. 6. (Color online) Robust transport of the power splitter. The field patterns of the z component of the electric field in the presence of defects with (a) a lightning-shaped opaque obstacle, (b) missing rods, (c) shifting rods, and (d) the combination. Insets: the zoom-in field patterns on the left of defects. The pseudospin-up source is used in the simulation.

triangular staggered photonic metacrystals with the trivial gap material [inset of Fig. 7(b)]. The pseudospin-momentum locked edge dispersion can be engineered by shifting the position of the first row of bianisotropic rods. The displacement of shifted rods from the unmodified lattice is denoted as s1, which is a positive number when shifting toward the trivial insulator. Figure 7(a) shows that the edge dispersion in the first lowest band gap becomes flat in the vicinity of $0.69(2\pi c/a)$ when $\mathrm{s1} = -0.26a$. This is different from the case of $\mathrm{s1} = 0$ [Fig. 3(b)], where no slow-light dispersion is found. We emphasize that such slow-light waveguide can manipulate the flow of light in a backscattering-free manner.

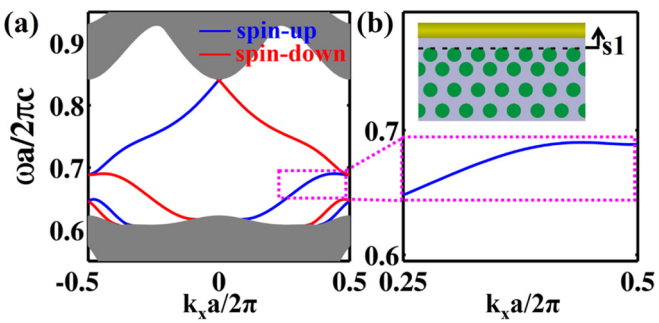

FIG. 7. (Color online) Robust slow-light waveguide. (a) The pseudospin-momentum locked edge dispersion in the first gap when $\mathrm{s1} = -0.26a$. Here s1 is the distance of the first row of bianisotropic rods from the unmodified lattice (black dashed line). Gapless pseudospin-polarized edge states are tailored by changing the morphology of edge. (b) Enlarged dispersion in the vicinity of the frequency of $0.69(c/a)$. The dispersion is flat and has the potential capability to realize slow-light waveguides.

The dispersion of such robust slow-light waveguide can be pursued to achieve a much slower group velocity and larger group index by further shifting the position of the second row of rods, or by adjusting the radius of the first two rows of rods.

E. Experimental proposal

Lastly, we discuss the experimental realization of the nontrivial staggered topological photonic metacrystal by employing a staggered split-ring array. Consider a bianisotropic photonic metacrystal whose unit cell is outlined by a hexagonal prism, depicted by the purple color in Fig. 8(a). The unit cell has one downward split ring embedded in air background. A split ring is made by a perfect electric conductor and provides large bianisotropy. However, since the material dispersions are different between the split ring (bianisotropic "rod," green hexagonal prism) and the air background, the pseudospin-up and pseudospin-down states are mixed together, as shown in Fig. 8(b). In contrast, the staggered topological photonic metacrystal is formed by split rings with opposite orientations instead of the air background. Figure 8(c) illustrates that the unit cell is constructed by one red downward and two blue upward split rings. Consequently, the inner green hexagonal region and the background region have uniform effective permittivity and permeability, while opposite bianisotropy. Thus the ε/μ-matching condition is fulfilled. The simulated band structure in Fig. 8(d) indicates that the pseudospin-up and pseudospin-down states are decoupled and almost overlapped at each k point. The slight shift at higher-order bands between two pseudospin polarizations is caused by the nonlocal effect. A nontrivial photonic band gap characterizing with $C_{s\text{-gap}} = 1$ ranges from $0.177(c/a)$ to $0.194(c/a)$. As a whole, the nontrivial staggered photonic metacrystal is

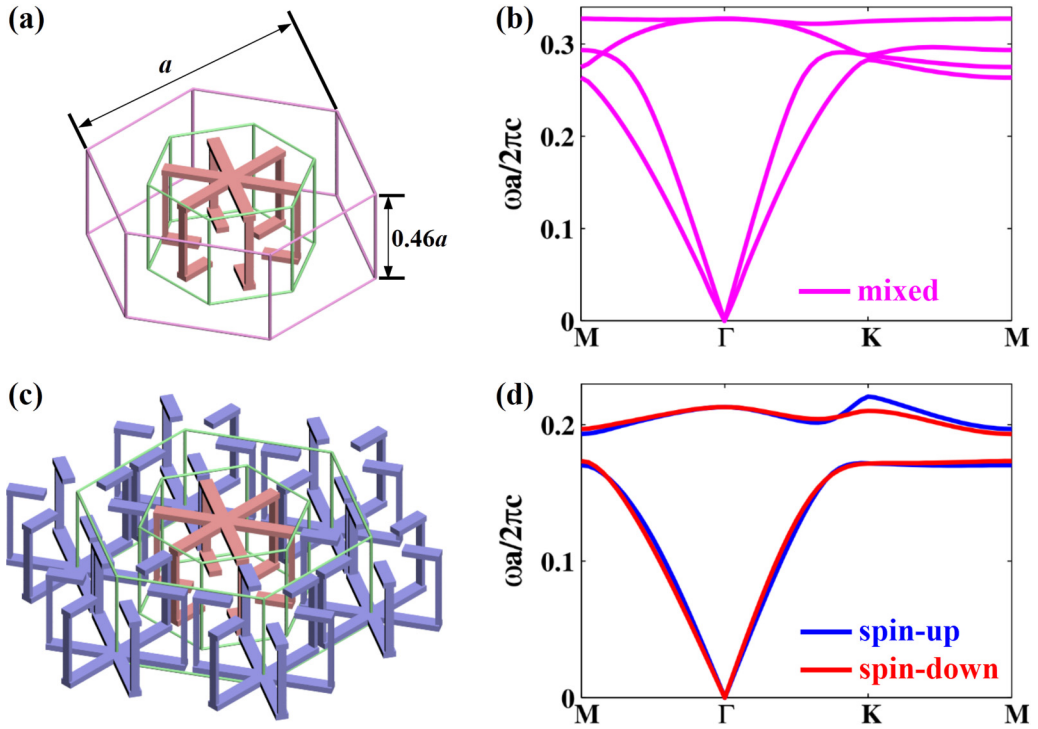

FIG. 8. (Color online) Experimental realization of the nontrivial staggered topological photonic metacrystal. (a) Bianisotropic photonic metacrystal with a unit cell of one downward split ring (red) embedded in air background. The sizes of the upper long, middle high, and lower short segments are $0.55a * 0.05a * 0.03a$, $0.02a * 0.03a * 0.37a$, and $0.14a * 0.05a * 0.03a$, respectively. The corresponding band structure is shown in (b), in which the pseudospin-up and pseudospin-down states are mixed together due to different material dispersions of split ring and air background. (c) Staggered photonic metacrystal constructed by split rings with same size but opposite orientation, i.e., downward in the "rod" (red), while upward in the "background" (blue). The corresponding band structure is shown in (d), in which the pseudospin-up and pseudospin-down states are decoupled, and they are almost overlapped at each k point, except a little bit of deviation at higher bands due to nonlocal effect. The nonzero Chern numbers of the lower bands demonstrate the nontrivial band gap from 0.177 to $0.194c/a$. See more in the text.

achieved and it may be readily realizable at microwave frequency.

IV. CONCLUSION

In conclusion, we propose a scheme to realize dispersion-immune photonic topological metacrystals. The material dispersions can be immune when the photonic metacrystals are constructed by materials with uniform permittivity and permeability but staggered bianisotropy. The ε/μ-matching condition is naturally fulfilled even for highly dispersive metamaterials. Such dispersion-immune concept is demonstrated in the triangular staggered photonic metacrystal. The pseudospin-momentum locked edge states are presented and a nontrivial band gap with a large gap spin Chern number is realized. A robust pseudospin-polarized power splitter and slow-light waveguide are discussed as examples of manipulating pseudospin-polarized states in dispersion-immune photonic topological insulators. In addition, the experimental proposal constructing by staggered spilt-ring metamaterials is also discussed.

ACKNOWLEDGMENTS

This work is supported by NSFC (Grant No. 11274396), Guangdong Distinguished Young Scholar (Grant No. S2013050015694), New Century Excellent Talents in University (Grant No. NCET-12-0607), and State Key Laboratory of Optoelectronic Materials and Technologies of Sun Yat-sen University.

[1] J. D. Joannopoulos, S. Johnson, J. Winn, and R. Meade, *Photonic Crystals: Molding the Flow of Light* (Princeton University Press, Princeton, NJ, 2008).

[2] J. Valentine, S. Zhang, T. Zentgraf, E. Ulin-Avila, D. A. Genov, G. Bartal, and X. Zhang, Nature (London) **455**, 376 (2008).

[3] S. Xi, H. S. Chen, B. Zhang, B. I. Wu, and J. A. Kong, Phys. Rev. B **79**, 155122 (2009).

[4] X. Q. Huang, Y. Lai, Z. H. Hang, H. H. Zheng, and C. T. Chan, Nat. Mater. **10**, 582 (2011).

[5] J. H. Shi, H. F. Ma, C. Y. Guan, Z. P. Wang, and T. J. Cui, Phys. Rev. B **89**, 165128 (2014).

[6] J. Lin, J. B. Mueller, Q. Wang, G. H. Yuan, N. Antoniou, X. C. Yuan, and F. Capasso, Science **340**, 331 (2013).
[7] L. Lu, J. D. Joannopoulos, and M. Soljačić, Nat. Photonics **8**, 821 (2014).
[8] F. D. M. Haldane and S. Raghu, Phys. Rev. Lett. **100**, 013904 (2008).
[9] Z. Wang, Y. D. Chong, J. D. Joannopoulos, and M. Soljačić, Phys. Rev. Lett. **100**, 013905 (2008).
[10] Z. Wang, Y. D. Chong, J. Joannopoulos, and M. Soljačić, Nature (London) **461**, 772 (2009).
[11] X. Y. Ao, Z. F. Lin, and C. T. Chan, Phys. Rev. B **80**, 033105 (2009).
[12] Y. Poo, R. X. Wu, Z. F. Lin, Y. Yang, and C. T. Chan, Phys. Rev. Lett. **106**, 093903 (2011).
[13] S. A. Skirlo, L. Lu, and M. Soljačić, Phys. Rev. Lett. **113**, 113904 (2014).
[14] A. B. Khanikaev, S. H. Mousavi, W. K. Tse, M. Kargarian, A. H. MacDonald, and G. Shvets, Nat. Mater. **12**, 233 (2013).
[15] W. J. Chen, S. J. Jiang, X. D. Chen, B. C. Zhu, L. Zhou, J. W. Dong, and C. T. Chan, Nat. Commun. **5**, 5782 (2014).
[16] T. Ma, A. B. Khanikaev, S. H. Mousavi, and G. Shvets, Phys. Rev. Lett. **114**, 127401 (2015).
[17] K. J. Fang, Z. F. Yu, and S. H. Fan, Nat. Photonics **6**, 782 (2012).
[18] M. Hafezi, E. A. Demler, M. D. Lukin, and J. M. Taylor, Nat. Phys. **7**, 907 (2011).
[19] M. Hafezi, S. Mittal, J. Fan, A. Migdall, and J. Taylor, Nat. Photonics **7**, 1001 (2013).
[20] G. Q. Liang and Y. D. Chong, Phys. Rev. Lett. **110**, 203904 (2013).
[21] M. C. Rechtsman, J. M. Zeuner, Y. Plotnik, Y. Lumer, D. Podolsky, F. Dreisow, S. Nolte, M. Segev, and A. Szameit, Nature (London) **496**, 196 (2013).
[22] M. C. Rechtsman, Y. Plotnik, J. M. Zeuner, D. H. Song, Z. G. Chen, A. Szameit, and M. Segev, Phys. Rev. Lett. **111**, 103901 (2013).
[23] L. Lu, L. Fu, J. D. Joannopoulos, and M. Soljačić, Nat. Photonics **7**, 294 (2013).
[24] W. L. Gao, M. Lawrence, B. Yang, F. Liu, F. F. Fang, B. Béri, J. Li, and S. Zhang, Phys. Rev. Lett. **114**, 037402 (2015).
[25] C. He, X. C. Sun, X. P. Liu, M. H. Lu, Y. L. Chen, L. Feng, and Y. F. Chen, arXiv:1405.2869.
[26] C. He, L. Lin, X. C. Sun, X. P. Liu, M. H. Lu, and Y. F. Chen, Int. J. Mod. Phys. B **28**, 1441001 (2014).
[27] M. Pasek and Y. D. Chong, Phys. Rev. B **89**, 075113 (2014).
[28] C. Fang, M. J. Gilbert, and B. A. Bernevig, Phys. Rev. B **86**, 115112 (2012).
[29] I. V. Lindell and A. H. Sihvola, J. Electromagn. Waves Appl. **19**, 861 (2005).
[30] H. M. El-Maghrabi, A. M. Attiya, and E. A. Hashish, Prog. Electromagn. Res. **16**, 159 (2011).
[31] C. A. Valagiannopoulos and A. H. Sihvola, Electromagnetics **34**, 593 (2014).
[32] Y. Hatsugai, Phys. Rev. Lett. **71**, 3697 (1993).
[33] See Supplemental Material at http://link.aps.org/supplemental/10.1103/PhysRevB.92.014210 for the functionality of the pseudospin-polarized power splitter on the input source.